

Low-grade wind driven directional flow in anchored droplets

Shan Peng^{a,1}, Binglin Xie^{b,1}, Yanlei Wang^{c,1}, Mi Wang^c, Xiaoxin Chen^a, Xiaoyu Ji^a,
Chenyang Zhao^a, Gang Lu^d, Dianyu Wang^e, Ruiran Hao^f, Mingzhan Wang^g, Nan Hu^{b, h,2},
Hongyan He^{c, i, 2}, Yulong Ding^j, Shuang Zheng^{k,2}

^aDepartment of Inorganic Chemistry, College of Chemistry and Materials Science, Key Laboratory of Medicinal Chemistry and Molecular Diagnosis of Ministry of Education, Key Laboratory of Analytical Science and Technology of Hebei Province, Hebei University, Baoding 071002, Hebei, China.

^bSchool of Civil Engineering and Transportation, South China University of Technology, Guangzhou 510641, China.

^cBeijing Key Laboratory of Ionic Liquids Clean Process, Institute of Process Engineering, Chinese Academy of Sciences, Beijing 100190, China.

^dDepartment of Biomedical Sciences, City University of Hong Kong, Hong Kong 000000, China

^eSchool of Chemical Engineering, Zhengzhou University, Zhengzhou 450001, China.

^fSchool of Environmental Engineering, Yellow River Conservancy Technical Institute, Kaifeng 475004, China.

^gPritzker School of Molecular Engineering, University of Chicago, Chicago 000000, Illinois, USA.

^hPazhou Lab, Guangzhou 510005, China.

ⁱLongzihu New Energy Laboratory, Zhengzhou Institute of Emerging Industrial Technology, Zhengzhou 451150, China.

^jSchool of Chemical Engineering, University of Birmingham, Birmingham 000000, United Kingdom.

^kDepartment of Civil Engineering, The University of Hong Kong, Hong Kong 000000, China.

¹S. P., B. X. and Y. W. contributed equally.

²Correspondence and requests for materials should be addressed to N. H. (Email: nanhu026@scut.edu.cn), H. H. (Email: hyhe@ipe.ac.cn) and S. Z. (Email: zhengshuang@iccas.ac.cn)

Author Contributions

S. Z. conceived the project. S. P. and S. Z. designed the research. S. P. conducted the experiments and collected the data. S. Z. and S. P. analyzed the experimental results. H. H. Y. W. and M. W. performed and drafted the MD simulation and theoretical analysis. B. X. and N. H. performed and drafted the CFD simulation and theoretical analysis. All authors contributed to this work. S. Z. and Y. D. revised the manuscript. S. Z., N. H. and H. H. supervised the research. S. P., B. X. and Y. W. contributed equally.

Methods

Fabrication method of the PDMS nanowire arrays. PDMS prepolymer hybrid (Dow Corning, Sylgard 184) was fabricated by blending prepolymer and its hardener in a mass ratio of 10: 1, then manually agitating for 10 min and continuously outgassing in vacuum for 30 min. The experimental setup was manufactured on the basis of Supplementary Fig. S7. Specifically, a piece of AAO template (2 cm \times 2 cm, pore diameter of 90 nm, Top membranes Inc.) was in sequence washed by deionized (DI) water, acetone, and ethanol (95%) for 10 min. We added two droplets containing 0.2 μ L conductive adhesive (SPI) and silver wires onto AAO template with the distance of 0.4 cm followed by curing at 80 $^{\circ}$ C for 2 h, and a sandpaper (P2000, Huaxin Company) was used to rub the solid Ag on the surface, enhancing the adhesion between solid Ag and PDMS substrate, which was fabricated *via* depositing 0.2 mL of PDMS prepolymer blend before solidifying at 90 $^{\circ}$ C for 3 h. Finally, AAO template was removed and PDMS nanowire arrays with finely embedded solid Ag was obtained. The setup was washed clean using water and ethanol for several times before chemical modifying. Ag/AgCl electrode was fabricated according to the device.

Preparation of DWG. PDMS nanowire array was activated by oxygen plasma (100 W) for 30 s and the activated PDMS was further submerged into a 3-methacryloxypropyl-trimethoxyssilane (MPS, Aladdin) solution (1 wt%) in absolute ethanol for 5 h to graft with MPS followed by rinsing for several times using absolute ethanol. Grafting reaction between sodium polystyrenesulfonate (PSS) and PDMS was achieved by free radical polymerization. The modified PDMS was firstly immersed into benzophenone (AR, Aladdin) ethanol solution (0.1 mol/L) for 20 min, then it was next submerged in aqueous sodium styrene sulfonate (AR, Aladdin) solution (5 wt%), and the whole system was placed under ultraviolet irradiation (PLS SXE 300 with xenon lamp, Perfect Light) with intensity of 70 mW/cm² for 1 h. Then the substrate was removed from the solution, washed repeatedly by DI water, and finally dried under the nitrogen flow. We added various water content into IL solution to mediate molar ratio between water and IL. To stabilize IL drop onto above-mentioned PSS grafted PDMS nanowire array substrate, a 75 μ L IL drop (1-Octyl-2-methylimidazolium chloride) was placed to the central electrode of the device,

which was exposed to moisture-saturated ambient air within a polymethyl methacrylate holder to guarantee adequate water absorption.

Characterization and voltage generation measurement. The morphology of the as-prepared samples was captured using a FEI Nova Nano SEM 430 system. X-ray photoelectron spectroscopy (XPS) surveys were measured on an Axis Ultra DLD spectrometer (Krayos, Shimadzu, Japan) with 1486.6 eV Al K α radiation. Surface elemental distribution of the treated sample was carried out using energy dispersive X-ray spectrometer (EDX, HORIBA, 7593-H). Contact angles in air were determined on an OCA35 at room temperature (Data Physics, Germany), which was averaged values of five measurements at various positions on each sample. Fourier-transform infrared spectroscopy (FTIR) spectrum was obtained on a Germany Bruker Tensor with an ATR attachment. The capillary flow behavior was carefully studied through adding PS microspheres (Sigma-Aldrich, diameter of $\sim 10\ \mu\text{m}$) into IL (1-Octyl-3-methyl imidazole chloride) followed by blending with hand for 10 min and ultraphonic treatment (Beijing Cpower, 5320DTH) for another 10 min. The movement processes of PS microspheres were recorded by an Optical microscope (Olympus BX51) connected with a computer. An analytical balance was used to measure the liquid water content and weight of IL droplet. The open-circuit power and short-circuit current of the DWG were measured using a digimer (DMM6500, Keithley Instruments). The ambient conditions around experimental device in diverse ways were regulated based on specific experiment requirements. For tests under different wind speed (Fig. 3), the device was positioned indoor environment with wind speed controlled by a blower with diverse power. The airflow speed was recorded in real time at diverse wind speed. For ambient requiring diverse humidity (Fig. 4), ultrasonic humidifier or CaCl₂ (AR, Aladdin) were used to control the humidity of the device confined in a closed container.

MD simulations

MD simulations of the sandwich structure (PDMS-IL-PDMS) was performed by the large-scale atomic/molecular massively parallel simulator (LAMMPS) (1). The space size occupied by ILs of the three systems ($x = 0, 4$, and 8) as research objects, is $45.0\ \text{\AA}$, $45.0\ \text{\AA}$, and $53.4\ \text{\AA}$ in three directions. The number of ILs and water molecules are summarized in Supplementary Table S1. Periodic boundary condition (PBC) was exerted along the

PDMS slab, while an open boundary condition was applied through the vertical panel direction. Interactions between water and PDMS are expressed by the SPC/E model (2) and CVFF force field (3), respectively. The force field of ILs is described by nonpolarizable all-atom optimized potentials for the liquid simulation (OPLS-AA) (4, 5) force field, which has been used successfully to describe the structure and properties of ILs. The geometric mixing rule was used to model the interatomic interactions. The long-range electrostatic interactions are computed by the particle-particle particle-mesh (PPPM) algorithm. Meanwhile, considering the effect of charge polarization, the charge of ILs is scaled by 0.8 times (6). Van der Waals (vdW) interactions are calculated by 12-6 Lennard-Jones potential. The cutoff is 1.2 nm for both coulombic and vdW interactions.

All systems are modeled at 300 K and the timestep is 2 fs. The ion number in the box was determined by using pressure and layer spacing. Then relax the system in the NVT ensemble at least 10 ns. Once the system is in equilibrium, 5 ns-long track data is collected for analysis. In the flow systems, different pressures are applied to water by the following formula

$$\Delta P = \frac{N \times f_0}{S} \quad (1)$$

where N is the total atomic number of water molecules in the system, f_0 is the force added, and S is the nanochannel cross-sectional area. The reduced pressure applied in this work are 0.22, 0.29, and 0.36 MPa, respectively.

CFD models

We built the CFD models for the internal circulation flow of droplets using the commercial software Fluent based on the ANSYS R19.0. We first created the geometry of the computational fluid domain using a rectangle of 100 mm \times 50 mm in the DesignModeler, and added a partially circular region for the droplet with a 10 mm diameter and contact angle of 62°. The contact angles varied in the parametric study, ranging from 11° to 51°. Then, we generated the unstructured mesh for the geometry using 260, 154 elements with a maximum face size of 0.2 mm as shown in Supplementary Fig. S11. The 2D geometries generation of droplets for our simplified CFD models can be performed as follows: Make a horizontal line segment AB, so that AB = 10 mm, which is equal to the length D of the contact line at the bottom of the droplet. Drawing the mid-perpendicular CE of line segment

AB. Plotting the line segment AD counterclockwise from point A, so that the size of \angle BAD is equal to the droplet contact angle. Create the vertical line of line segment AD from point A, to obtain the intersection point O with the extension line of CE. Taking point O as the center and the radius of OA as the circle, the "partial circular ABC" divided by the chord AB is obtained as the simplified geometry of the droplet for CFD model calculation. Then the droplet height can be approximated by the following formula:

$$L_y = \frac{D_x(1-\cos \theta_L)}{2 \sin \theta_L} \quad (2)$$

Specific material properties are selected as follows: the density of air is 1.225 kg/m^3 and the viscosity of air is 0.017894 cP . The density and viscosity of the droplet are 1000 kg/m^3 and 337 cP , respectively. The interfacial tension coefficient is 0.0338 N/m , the diameter of the contact surface is 10 mm , and the contact angle of the adhered droplet is 62° .

We adopted the laminar and multiphase model to solve conservation equations for gas and liquid phases, volume fraction in each cell is then calculated, and the mixture density and the mixture viscosity are given by Equation 3 and Equation 4.

$$\rho = \beta_2 \rho_2 + (1 - \beta_2) \rho_1 \quad (3)$$

$$\mu = \beta_2 \mu_2 + (1 - \beta_2) \mu_1 \quad (4)$$

Where subscripts 1 and 2 mean the fluid properties of the gas/liquid phase respectively for our problem. β_2 and $(1 - \beta_2)$ refer to the volume fraction of the liquid/gas phases, solved by the following equation:

$$\frac{\partial \alpha_2}{\partial t} + v \cdot \nabla \beta_2 = 0 \quad (5)$$

Continuous phase volume fraction was calculated using the following conservation equation:

$$\sum_{q=1}^n \beta_q = 1 \quad (6)$$

The volumetric surface tension force in Equation 3 in main paper is defined by the continuum surface force (CSF) model (7) as follows:

$$f = \frac{\rho}{0.5(\rho_1 + \rho_2)} \sigma k \nabla \beta_2 \quad (7)$$

Where σ is the surface tension coefficient. And the curvature k is the divergence of the unit normal (\hat{n}) at the interface:

$$k = \nabla \cdot \hat{n} \quad (8)$$

where

$$\hat{n} = \frac{\vec{n}}{|\vec{n}|} \quad (9)$$

and the surface normal vector, \vec{n} is gradient of the phase volume fraction β_2 as:

$$\vec{n} = \nabla \beta_2 \quad (10)$$

For the benchmark model with $\alpha = 0^\circ$, the “velocity-inlet” of airflow is set as 2 m/s on the right-hand side of the computing domain, and the “pressure-outlet” is used on the left-hand side. The upper and lower edges are the walls. For the model with $\alpha = 90^\circ$, the upper edge of the wind field has a velocity-inlet of 2 m/s, and both the left and right sides are the pressure-outlet, and the static bottom edge is the wall. While for the model with $\alpha = 180^\circ$, the left side of the computational region is the velocity-inlet of wind with 2 m/s, the right outlet is the pressure-out, and the upper and lower edges are the walls.

We used the pressure-based type of solver, with the gravitational acceleration of 9.81 m/s² in the y-direction. We selected the PISO scheme and the Least-Squares cell-based scheme to calculate the Pressure–velocity coupling, and the gradient, respectively. We implemented the first-order upwind scheme, the Geo-Reconstruct, the Presto schemes, and the First Order Implicit to discretize the momentum equation, the volume fraction, the pressure, and the transient formulation, respectively. We initialized the solution using the hybrid method and patched the value of volume fraction to 1 for the liquid phase. After the solutions are completed, we analyzed and visualized our results in CFD-Post software.

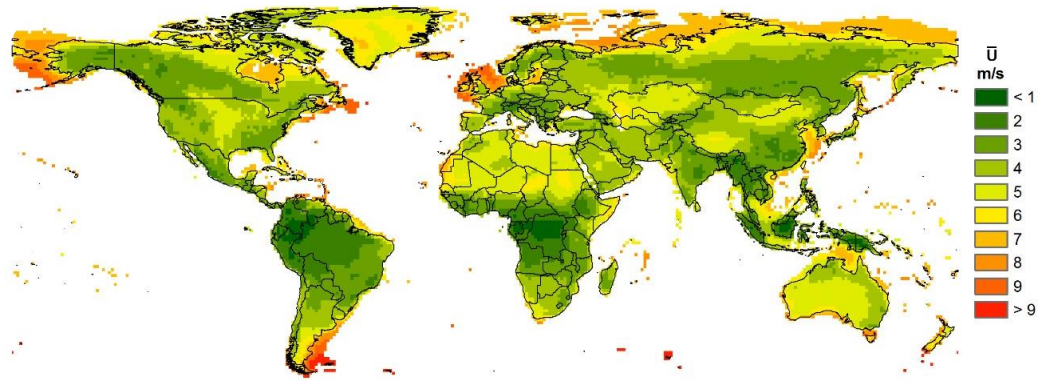


Figure S1. Global wind velocity distribution in the world (8). V_{wind} less than 5 m/s are far more extensively distributed in the world. (The picture is altered minimally with permission from ref. (8), Elsevier).

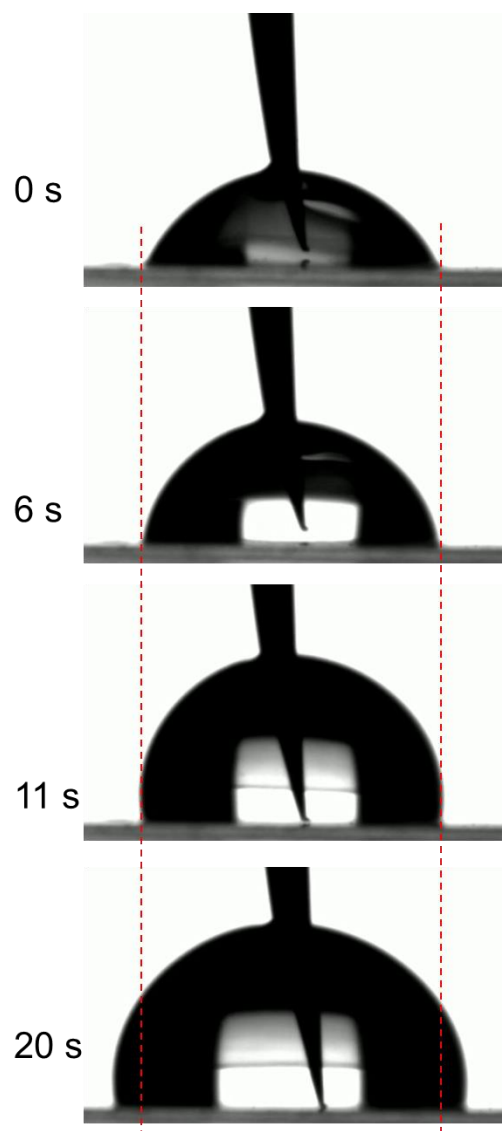


Figure S2. Continuous imaging of TCL pinning on nanowire array when keep adding IL into the drop. Water content $w_{\text{H}_2\text{O}}$ is 23.3% under the RH of $\sim 40\%$.

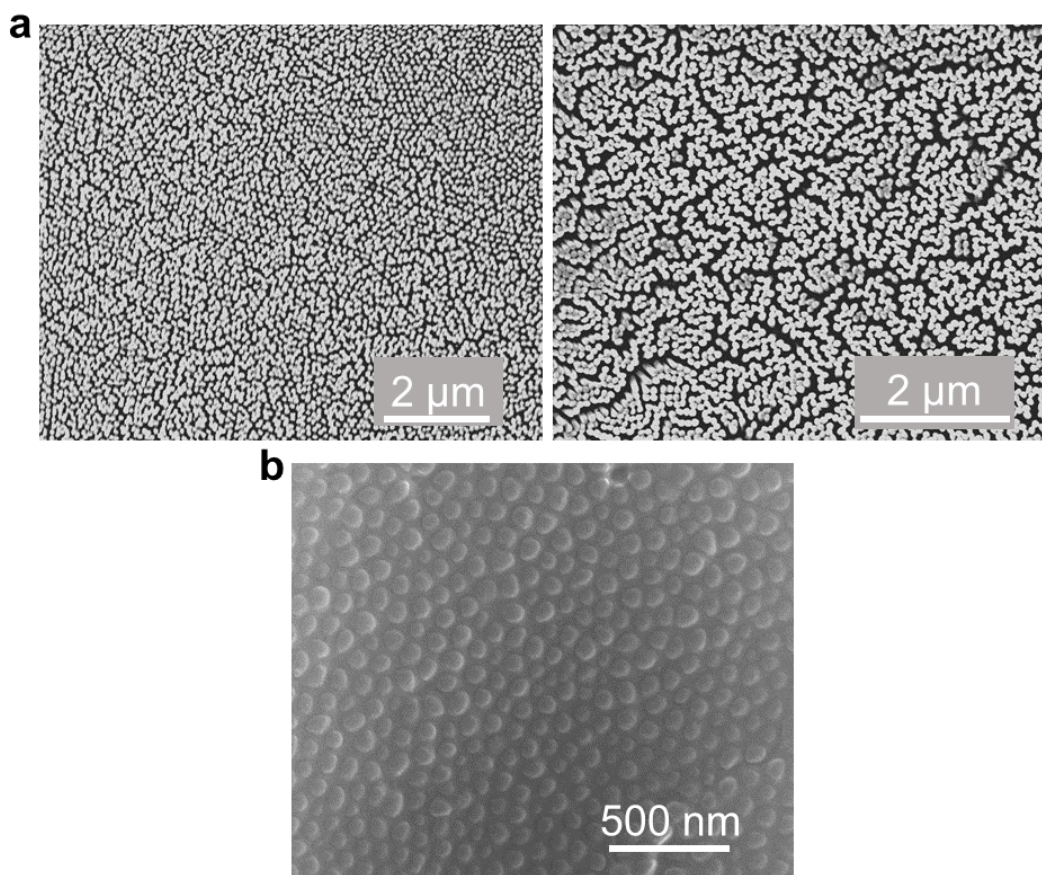


Figure S3. Morphology characterization of PSS grafted PDMS nanowire array. a, Low- and high-magnification SEM images for PDMS nanowire arrays after grafted with PSS brushes, which is used for diameter measurement. b, Much Higher-magnification SEM image for PSS grafted PDMS nanowire arrays filled with IL (1-Octyl-3-methylimidazolium chloride) to determine the center-to-center spacing.

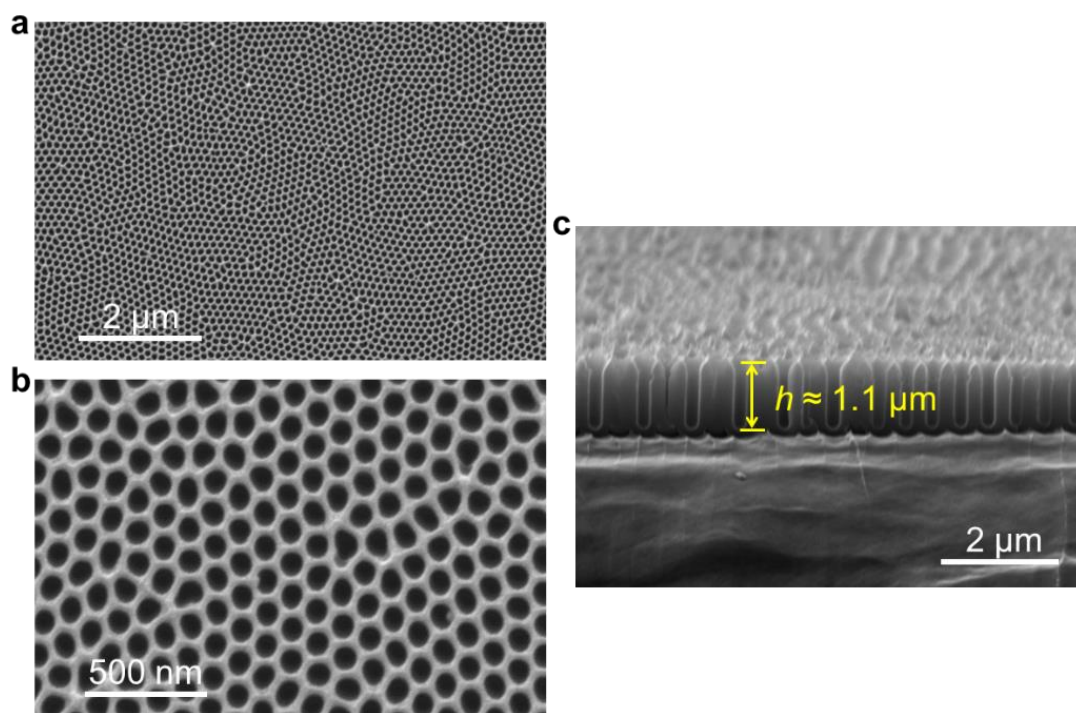


Figure S4. Morphology characterization of AAO template. a-b, Low and high-magnification topical SEM images. c, Side-view SEM image of AAO template.

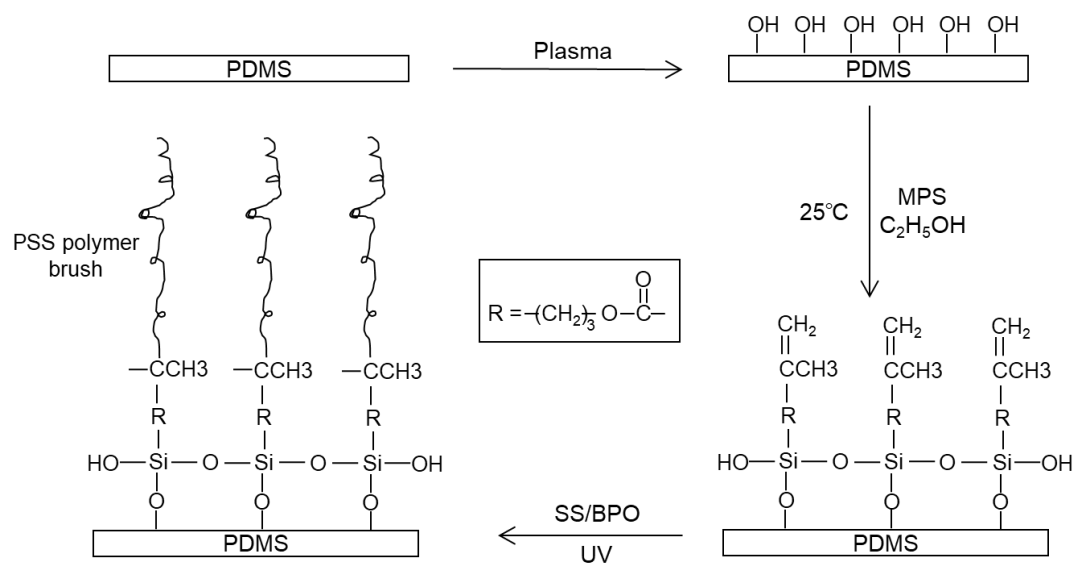


Figure S5. Grafting strategy of PSS brushes onto PDMS nanowires. The PSS brushes are successfully grafted onto PDMS nanowire arrays through free radical polymerization.

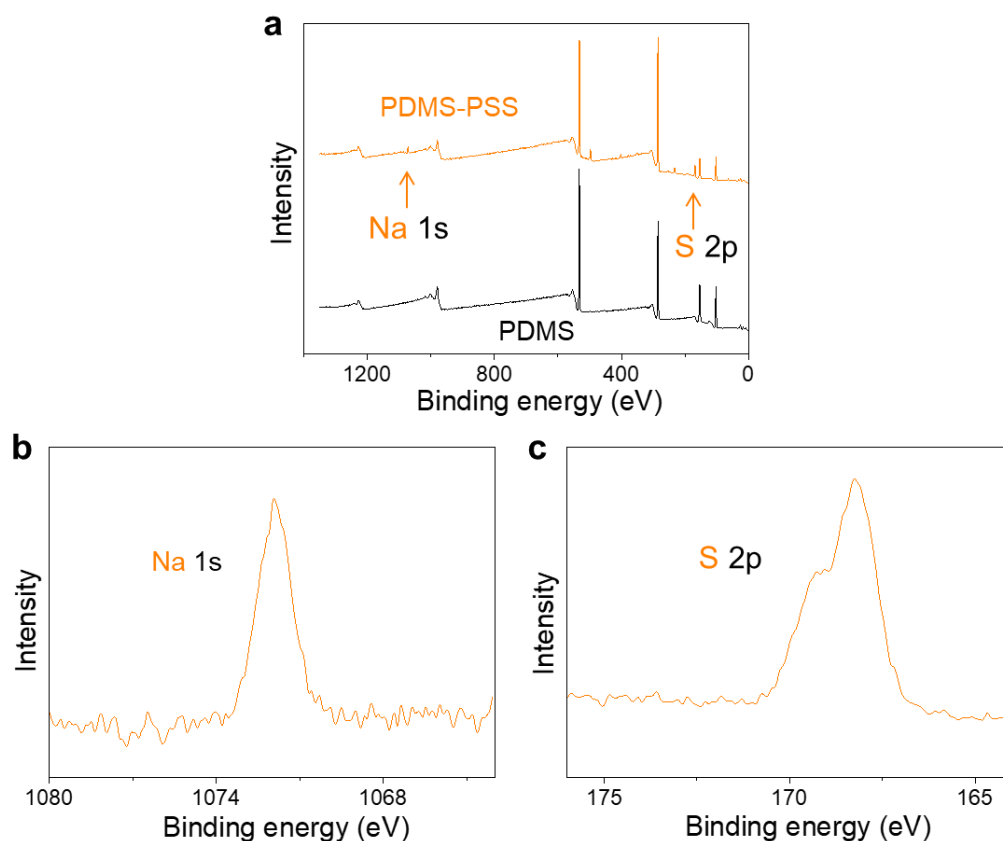


Figure S6. XPS characterization of PSS grafted PDMS nanowire arrays. a, X-ray photoelectron spectroscopy (XPS) full spectra of PDMS nanowires before and after grafted with PSS brushes. b-c, Demonstration of PSS grafted PDMS nanowires, suggested by characteristic Na 1s and S 2p peaks.

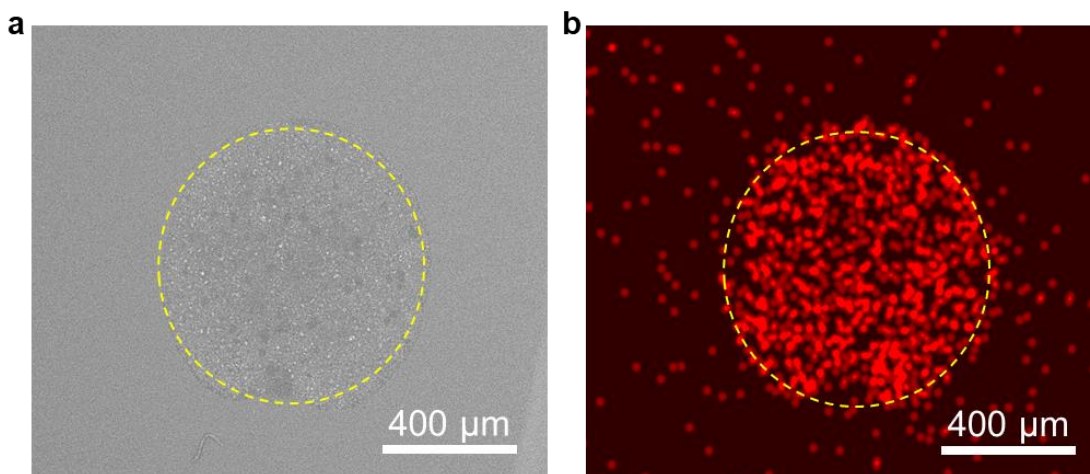


Figure S7. Morphology and EDS mapping images of electrode. a, Low-magnification SEM image of the electrode area marked by the yellow dotted line. b, Certification of Ag element distribution by EDS mapping.

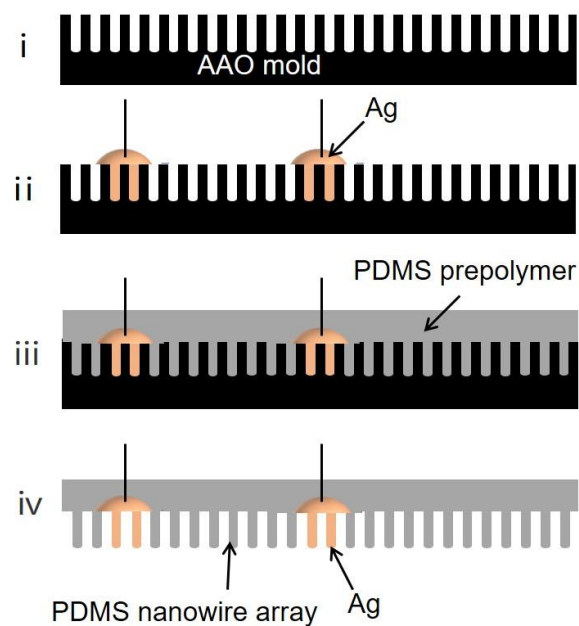


Figure S8. Preparation strategy of the PDMS nanowires with electrode. AAO template (i) with regular pore distribution was filled with droplets containing 0.2 μL conductive adhesive (SPI) and silver wires followed by curing at 80 $^{\circ}\text{C}$ for 2 h (ii). Then 0.2 mL of PDMS prepolymer blend was deposited onto AAO mold and was further solidified at 90 $^{\circ}\text{C}$ for 3 h (iii). Finally, the AAO template was removed (iv).

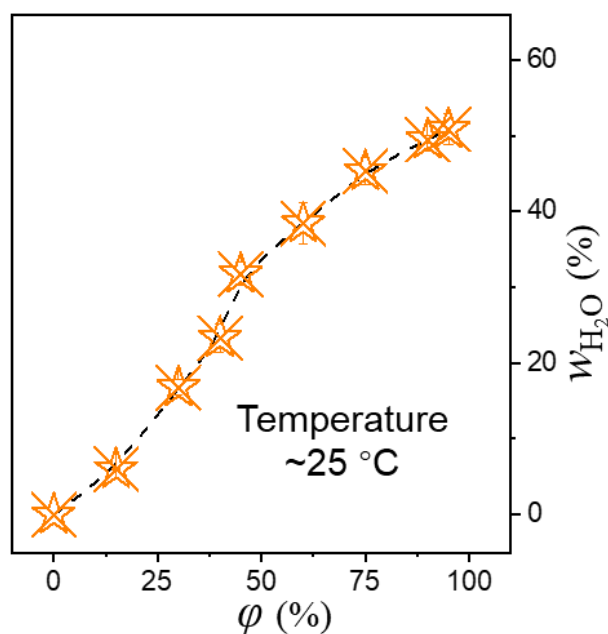


Figure S9. Relationship between water content $w_{\text{H}_2\text{O}}$ and relative humidity ϕ at the temperature of 25 °C. $w_{\text{H}_2\text{O}}$ is increased with the increase of ϕ . (The data is minimally modified with permission from ref. (9), Wiley).

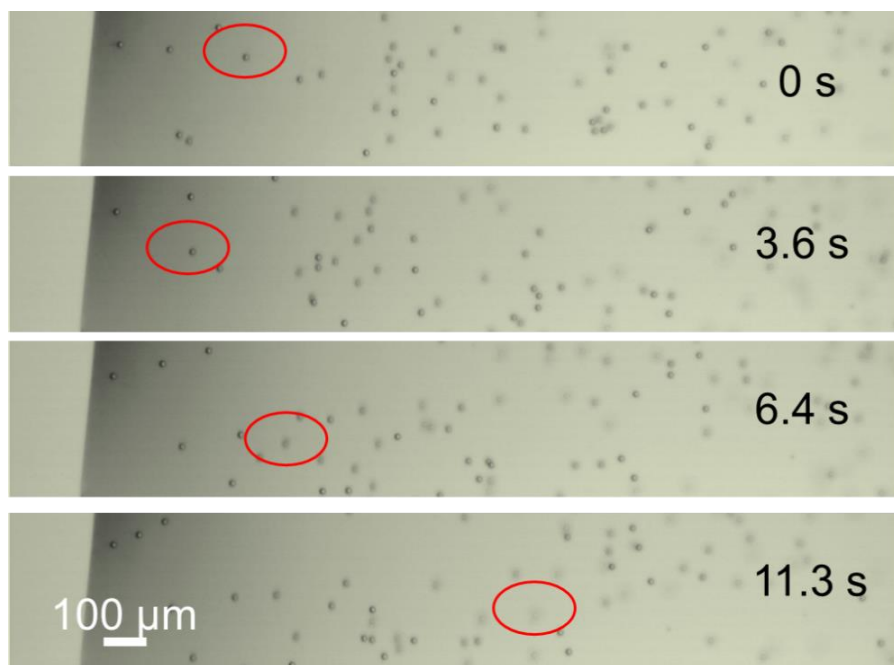


Figure S10. Microscope recording of circulating flow under wind direction $\alpha = 180^\circ$. *In-situ* microscope recording of PS microspheres added to IL drop ($w_{\text{H}_2\text{O}} = 23.3\%$) under $V_{\text{wind}} \approx 2 \text{ m/s}$ to demonstrate the circulating flow induced by airflow $\alpha = 180^\circ$.

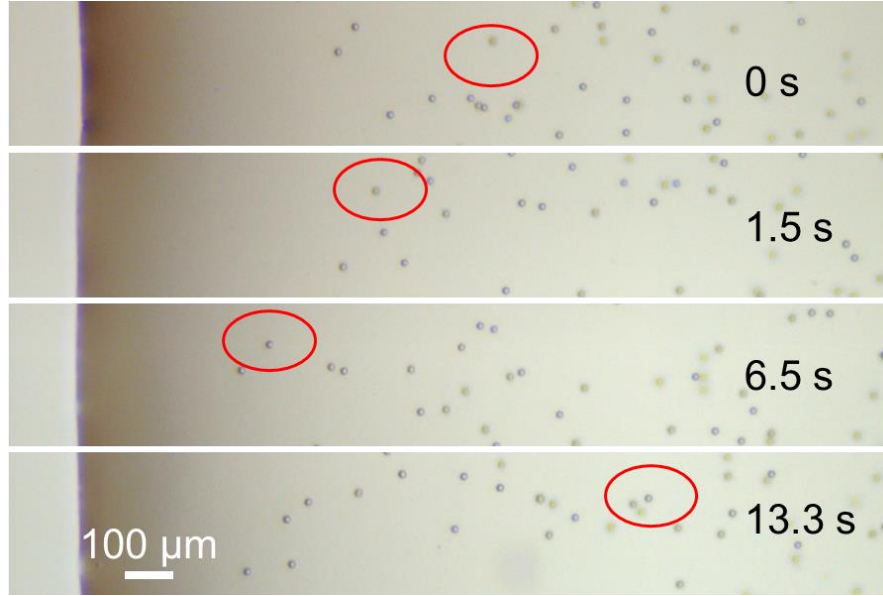


Figure S11. Microscope recording of circulating flow under wind direction $\alpha = 90^\circ$. *In-situ* microscope recording of PS microspheres added to IL drop ($w_{\text{H}_2\text{O}} = 23.3\%$) under $V_{\text{wind}} \approx 2$ m/s with the airflow perpendicular to the substrate ($\alpha = 90^\circ$).

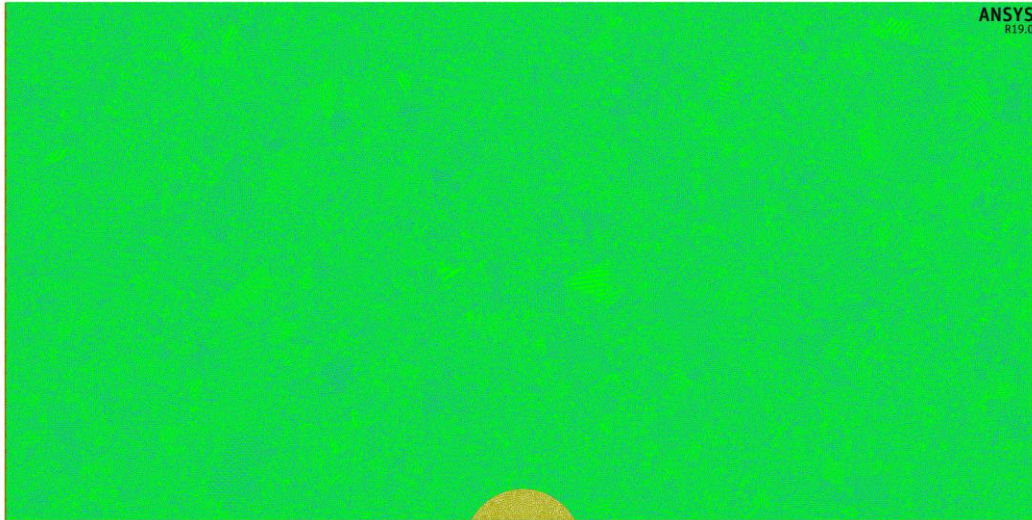


Figure S12. The geometry and grids of the computational fluid domain.

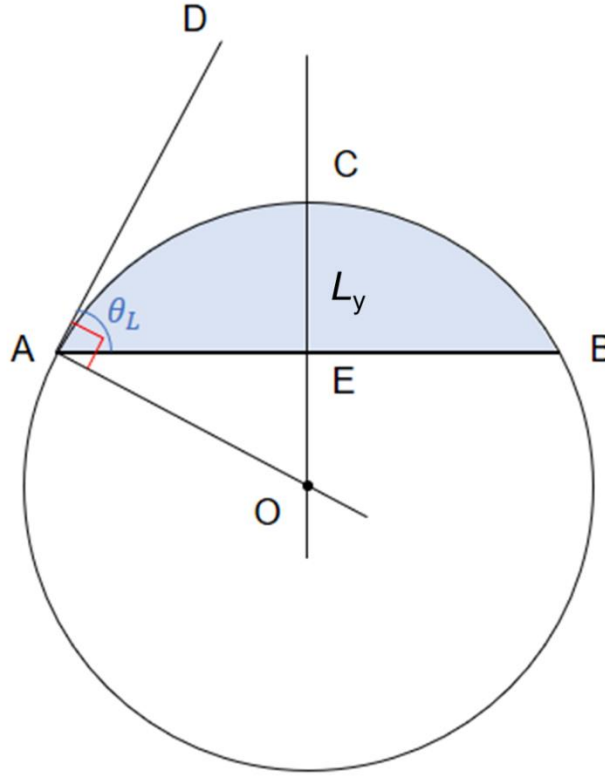


Figure S13. The generation of droplet geometries for our simplified CFD models.

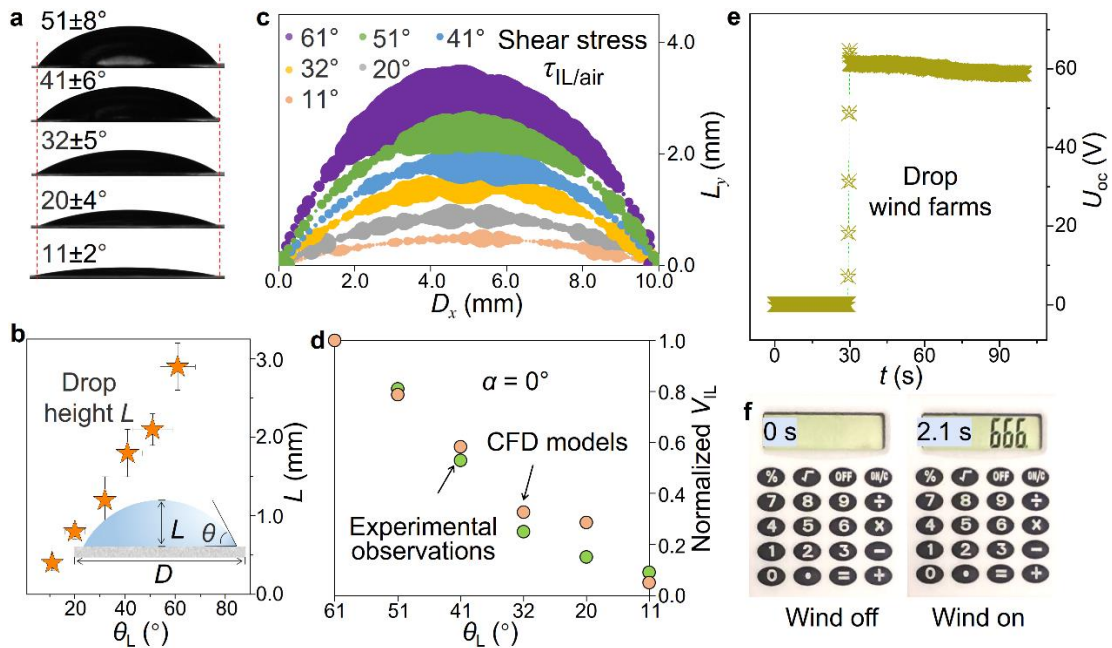


Figure S14. Contact angles (CAs) mediated internal circulation and applications as drop wind farms. a, Profile of droplets with various CAs (θ_L). b, The relationship between drop

height L and θ_L . c, The shear stress distribution on the surface of droplet under airflow with $\alpha = 0^\circ$ for various θ_L . d, The average velocity at the bottom surface of the drop decreases linearly with the reduction of θ_L for $\alpha = 0^\circ$ in our experimental and CFD model observations. e, Voltage output from a series drop wind farm containing $9 * 9$ drops. f, Snapshots of wind-induced LCD screen on and off ([Movie S5](#)).

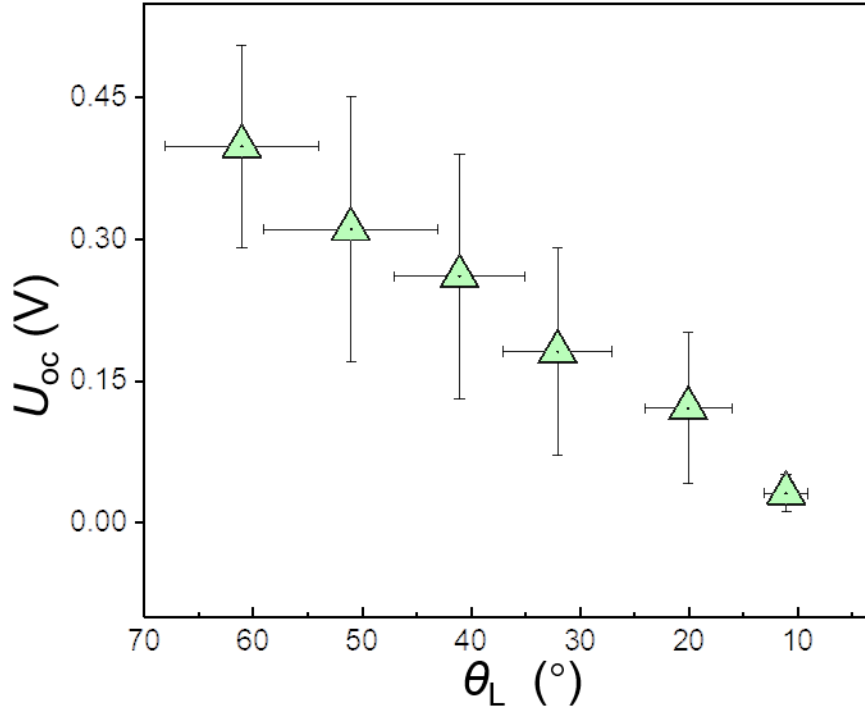


Figure S15. U_{oc} dependence of droplet CA. Experiments implemented under $V_{wind} = 2$ m/s and $w_{H_2O} = 23.3\%$.

Table S1 The number of IL and H_2O in different interface systems.

$x(H_2O)$	0	4	8
IL	250	214	181
H_2O	0	856	1448

Movie S1. Variation process of CAs when continuously adding IL into the drop.

Movie S2. Circulation process of PS microspheres under wind direction $\alpha = 0^\circ$.

Movie S3. Circulation process of PS microspheres under wind direction $\alpha = 180^\circ$.

Movie S4. Circulation process of PS microspheres under wind direction $\alpha = 90^\circ$.

Movie S5. On and off of drop wind farms powering LCD screen.

SI References

1. S. Plimpton, Fast parallel algorithms for short-range molecular dynamics. *J. Comput. Phys.* **117**, 1-19 (1995).
2. S. Chowdhuri, M. L. Tan, T. Ichiye, Dynamical properties of the soft sticky dipole-quadrupole-octupole water model: a molecular dynamics study. *J. Chem. Phys.* **125**, 144513 (2006).
3. F. Ritschl et al. An extension of the consistent valence force field (CVFF) with the aim to simulate the structures of vanadium phosphorus oxides and the adsorption of n-butane and of 1-butene on their crystal planes. *Z. Anorg. Allg. Chem.* **628**, 1385-1396 (2002).
4. M. Wang et al. Abnormal enhanced free ions of ionic liquids confined in carbon nanochannels. *J. Phys. Chem. Lett.* **12**, 6078-6084 (2021).
5. B. Li, C. Wang, Y. Zhang, Y. Wang, High CO₂ absorption capacity of metal-based ionic liquids: a molecular dynamics study. *Green Energy Environ.* **6**, 253-260 (2021).
6. J. Tang et al. Circadian humidity fluctuation induced capillary flow for sustainable mobile energy. *Nat. Commun.* **13**, 1291 (2022).
7. J. U. Brackbill, D. B. Kothe, C. Zemach, A continuum method for modeling surface tension. *J. Comput. Phys.* **100**, 335-354 (1992).
8. C. Jung, D. Schindler, Changing wind speed distributions under future global climate. *Energy Convers. Manage.* **198**, 111841 (2019).
9. S. Zheng et al. Continuous energy harvesting from ubiquitous humidity gradients using liquid-infused nanofluidics. *Adv. Mater.* **34**, 2106410 (2022).